ACCSCIENCE PUBLISHING

International Journal of Bioprinting

RESEARCH ARTICLE

Microstructure evolution and ductility improvement of additively manufactured biodegradable zinc–magnesium alloys via annealing

Changjun Han[1], Jinmiao Huang[1], Xiangling Ye[2], Boxun Liu[3]*, Zhi Dong[1], Yongqiang Yang[1], Junqing Gao[4,5], Kuangyang Yang[4,5]*, and Guocai Chen[4,5]*

[1]School of Mechanical and Automotive Engineering, South China University of Technology, Guangzhou, Guangdong, China

[2]Dongguan Hospital, Guangzhou University of Chinese Medicine, Dongguan, Guangdong, China

[3]Huamei Biotech Co. Ltd., Shenzhen, Guangdong, China

[4]Foshan Hospital of Traditional Chinese Medicine, Foshan, Guangdong, China

[5]The Eighth Clinical Medical College, Guangzhou University of Chinese Medicine, Foshan, Guangdong, China

***Corresponding authors:**
Boxun Liu
(bob@hmcell.com)

Kuangyang Yang
(dr.yky@163.com)

Guocai Chen
(chengc@fshtcm.com.cn)

Citation: Han C, Huang J, Ye X, et al. Microstructure evolution and ductility improvement of additively manufactured biodegradable zinc-magnesium alloys via annealing. *Int J Bioprint*. 2024;10(4):3034. doi: 10.36922/ijb.3034

Received: February 27, 2024
Accepted: March 26, 2024
Published Online: May 8, 2024

Abstract

Zinc–magnesium (Zn–Mg) alloys, fabricated by laser powder bed fusion (LPBF) additive manufacturing techniques, have emerged as promising candidates for biomedical implants due to their biodegradation capability, superior mechanical strength, and excellent biocompatibility. However, LPBF-fabricated Zn–Mg alloys still face challenges related to extremely low ductility and limited exploration of degradation characteristics. In this study, the impact of Mg incorporation on the printability, degradation properties, microstructure, and mechanical properties of LPBF-fabricated Zn–Mg alloys was primarily investigated. Furthermore, we proposed a viable annealing post-processing route for the first time to tailor the microstructural characteristics of the fabricated Zn–Mg alloy and enhanced its limited ductility. The results demonstrated that by applying a laser power of 80 W and a scanning speed of 600 mm/s, the relative density of LPBF-fabricated Zn–Mg alloy reached 98.62%. Increasing the Mg amount from 1 to 5 wt% refined the grain size while promoting an increase in Mg_2Zn_{11} and $MgZn_2$ phases. Among these compositions, the Zn–1Mg alloy exhibited the greatest degradation rate at 0.126 mm/year. The annealing treatment facilitated the microstructure evolution of the Zn–1Mg alloy, resulting in equiaxed grains, increased average grain size, high-angle grain boundaries, and enrichment of Mg at grain boundaries. After annealing at 300°C for 0.5 h, the tensile strength of Zn–1Mg alloy decreased from 254.92 to 170.93 MPa, while the elongation significantly increased by a factor of 14.3 from 0.55% to 8.43%. These findings provide valuable insights into an effective post-processing approach for tailoring the microstructure and resultant mechanical properties of LPBF-fabricated Zn and its alloys.

Keywords: Zinc alloys; Zinc–magnesium; Laser powder bed fusion; Annealing; Additive manufacturing

1. Introduction

Zinc (Zn) is a biodegradable metal material with extensive potential applications in cardiovascular stents, body sutures, and temporary porous bone implants.[1,2] Compared to other biodegradable metallic materials, including magnesium (Mg) and iron, Zn exhibits a moderate degradation rate and excellent biocompatibility without the release of hydrogen gas during degradation and lacks ferromagnetism that prevents interference with medical imaging devices.[3–5] However, the utilization of pure Zn implants is challenged by their insufficient mechanical strength for load-bearing applications, thus limiting the broader medical applications of Zn.[6,7] The incorporation of Mg into the pure Zn matrix to develop Zn–Mg alloys enables various strengthening mechanisms, resulting in improved mechanical strength of the Zn matrix.[8,9] Additionally, the generation of Mg ions during the degradation process of these alloys can promote cell proliferation and facilitate bone regeneration.[10–12]

Traditional manufacturing processes, including casting and powder metallurgy, have been extensively employed to prepare Zn–Mg alloys.[13–15] However, it is challenging to achieve precisely controllable interconnected microporous structures that can facilitate physiological activities, such as cell or bone tissue growth and fluid circulation.[16–18] Laser powder bed fusion (LPBF) offers notable advantages in fabricating implants with intricate internal structures and personalizes design features layerwise.[19,20] During LPBF processing of Zn–Mg alloys, the high energy density laser beam induces the Marangoni convection effect, enabling a homogeneous distribution of Mg within the Zn matrix.[21] The rapid heating and cooling rates, accompanied by substantial temperature gradients, effectively inhibit grain growth of Zn–Mg alloys, resulting in refined microstructures that further enhance their mechanical performance.[22] Currently, addressing the low melting point of Zn (419.53°C), which is proximate to its boiling point (907°C), remains a key challenge associated with LPBF processing of Zn–Mg alloys.[23] Excessive energy density can cause molten pool spattering and severe evaporation, while insufficient energy density leads to inadequate fusion of metal powders and pore formation.[24] Therefore, the control of process parameters is crucial in the fabrication of Zn–Mg alloy implants with refined grains, superior mechanical properties, and intricate porous structures.

Previous studies have documented the utilization of LPBF-fabricated Zn–Mg alloys. Ning et al.[25] explored the impact of 3 wt% Mg on the microstructure and mechanical performance of LPBF-fabricated Zn–Mg alloy. The findings revealed that the fabricated Zn–3Mg (density: 95.99%) sample exhibited enhanced microhardness (115.29 HV), tensile strength (197.54 MPa), and corrosion resistance compared to its Zn counterparts. Yang et al. used LPBF to print Zn–Mg alloys with 1–4 wt% Mg. Among these compositions, Zn–3Mg alloy demonstrated superior tensile strength at 220 MPa along with an elongation of 7.2%.[26] Qin et al.,[27] employing Zn–xMg prealloyed powders (x = 0, 1, 2, and 5 wt%), achieved relative densities exceeding 99.5%, demonstrating that the Mg incorporation resulted in refined grain sizes and the formation of fragile phases, such as Mg_2Zn_{11} and $MgZn_2$; notably, the highest tensile strength was observed for the Zn–1Mg alloy at 381 MPa with an elongation of 4.2%. However, both Zn–2Mg and Zn–5Mg exhibited reduced tensile strengths by 25.7% and 83.2%, respectively, accompanied by nearly negligible elongation values. Furthermore, a slight increase in Mg concentration increased the corrosion rate of Zn–Mg alloys. Despite notable advancements in the mechanical strength of LPBF-fabricated Zn–Mg alloys, the limited ductility and degradation characteristics still hinder their applications in implants.

Heat treatment is a viable approach to significantly enhance the mechanical performance of metallic materials while preserving their original composition.[28,29] This study investigated the influence of Mg addition on the microstructure and mechanical properties of Zn–Mg alloys (Mg concentration: 1, 3, and 5 wt%) fabricated by LPBF, followed by annealing via heat treatment. Optimal process parameters were determined for each Mg concentration to achieve nearly full and dense Zn–Mg alloys, and the *in vitro* degradation behavior of these samples was examined. Subsequently, heat treatment parameters for a representative LPBF-fabricated Zn–Mg alloy were identified, leading to a significant enhancement in its ductility. Finally, the mechanisms underlying microstructure evolution and ductility enhancement in the annealed Zn–Mg alloy were discussed.

2. Methods

2.1. Preparation of raw materials

The mechanical-mixed Zn–Mg powders, with Mg concentrations of 1, 3, and 5 wt%, were used as raw materials from spherical Zn and Mg elemental powders with various ratios due to the advantages of flexibility in adjusting Zn/Mg ratios and lower cost.[30] The Zn powders were supplemented with 1, 3, and 5 wt% of Mg powder, respectively, maintaining a ball-to-material ratio of 10:1, while rotating at a speed of 250 rpm for 1 h. The particle size of the powders was in the range of 15–53 μm. The morphology of the Zn–3Mg powder under a scanning electron microscope (SEM, FEI Nova nano 430, Netherlands) revealed predominantly spherical particles with smooth surfaces and minimal satellite particles adhered, indicating excellent flowability (Figure 1a).

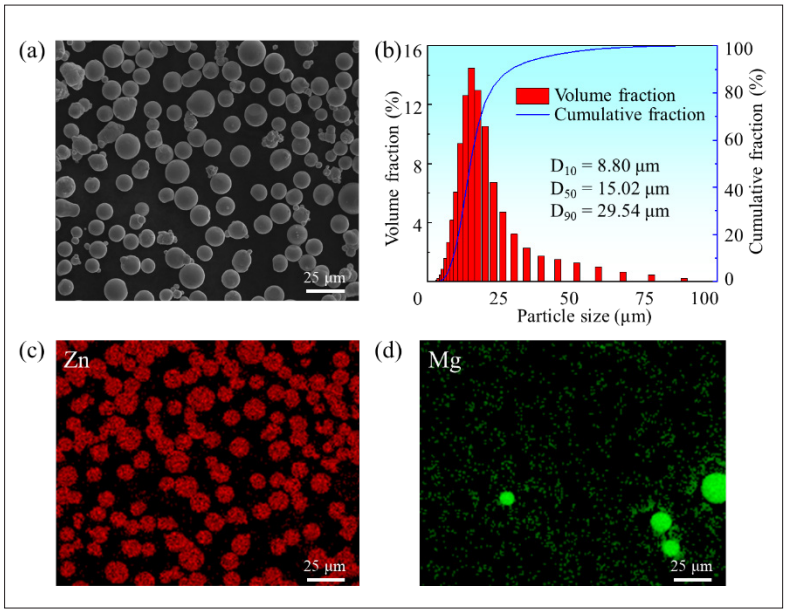

Figure 1. Characteristics of the Zn–Mg powder: (a) scanning electron microscope (SEM) images depicting the morphology of the raw powder; (b) particle size distribution; and (c and d) energy-dispersive X-ray spectroscopy (EDS) mapping, indicating the distribution of (c) Zn and (d) Mg.

Furthermore, Figure 1b presents the particle size distribution: D_{10} of 8.80 μm, D_{50} of 15.02 μm, and D_{90} of 29.54 μm. The element distribution for the Zn–3Mg powder is presented in Figure 1c and d, validating the presence of Mg.

2.2. Laser powder bed fusion process

The Zn–Mg powders were fabricated using a DiMetal-100 LPBF machine (Laseradd, China), which possessed a maximum laser power of 200 W. The volume energy density (Ev) was calculated based on laser power, scanning speed, layer thickness, and hatch space. Based on our preliminary experiments, hatch space and layer thickness values were set as 55 and 30 μm, respectively, while laser power and scanning speed values were varied to generate 30 different parameter combinations, as listed in Table 1. The dimensions of LPBF-fabricated Zn–Mg cubic samples were 8 × 8 × 4 mm^3. The tensile sample with dimensions of 72 × 22 × 3 mm^3 is depicted in Figure 2a. A bidirectional orthogonal scanning was employed, starting at an angle of 45° and rotating by an angle of 90° between consecutive layers, as schematically presented in Figure 2b. To ensure minimal oxygen content during the fabrication process, vacuum conditions with argon filling were implemented.

2.3. Annealing/heat treatment

According to experimental and equilibrium calculations of phase fractions, the LPBF-fabricated Zn–Mg alloys primarily comprise α-Zn and $MgZn_2$ phases, which

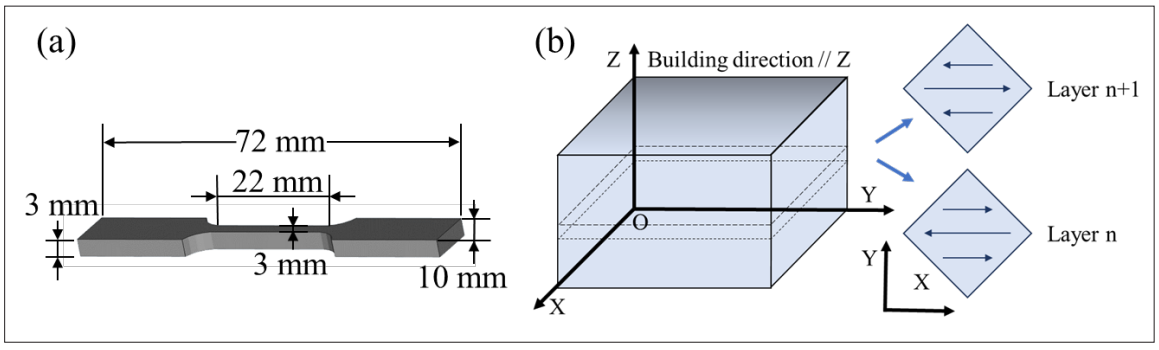

Figure 2. Fabrication of Zn–Mg samples: (a) tensile sample model and its dimensions, and (b) schematic of the scanning strategy.

Table 1. Laser powder bed fusion (LPBF) process parameters for printing Zn–Mg samples

Parameters	Value
Laser power (W)	50, 60, 70, 80, 90
Scanning speed (mm/s)	400, 500, 600, 700, 800, 900
Hatch space (μm)	55
Layer thickness (μm)	30

was consistent with the phase composition observed in casted Zn–Mg alloys. Figure 3a depicts the phase diagram of Zn–Mg alloys with Mg concentration. It could be inferred that the solubility of Mg within the Zn matrix is extremely limited (0.16 wt% at 364°C, but only 0.008 wt% at room temperature), leading to the formation of Mg_2Zn_{11} intermetallic phase even at low Mg concentrations. The diagram also indicated a eutectic point corresponding to approximately 3 wt% Mg, where a eutectic reaction occurred as expressed by:

$$MgZn_2 + L \rightarrow Mg_2Zn_{11} \quad (1)$$

The temperature range for the formation of Mg_2Zn_{11} is between 354.3 and 367.2°C.[29] However, it could be observed that this eutectic reaction is hindered when the Mg concentration in Zn–Mg alloys falls below 3%.[31] A series of preliminary experiments were conducted based on conventional heat treatment parameters (e.g., at 360°C for 15 h and 370°C for 10 h).[28,29,32,33] Subsequently, LPBF-fabricated Zn–Mg alloys underwent annealing at a temperature of 365°C for durations of 6, 10, and 14 h. These alloys exhibited relatively low tensile strength (100–120 MPa) and ductility (0.7–1%). Consequently, nine sets of annealing/heat treatment parameters were designed, involving different holding temperatures and durations at three distinct temperatures (Figure 3b). A vacuum sintering furnace (GJC-SJ300, Zhuzhou Guangjichang Technology Co., Ltd., China) was employed for annealing after sanding all surfaces of the as-built Zn–Mg alloy samples. Each set of annealing processes had a ramp rate of 10°C/min and cooling with a furnace.

2.4. Characterization

The relative density of LPBF-fabricated Zn–Mg alloys was determined using the Archimedes method after sanding all surfaces. Prior to microscopic characterization, Zn–Mg cubic samples were immersed in anhydrous ethanol, subjected to ultrasonic cleaning, and then underwent sandpaper grinding (grit sizes: 180, 400, 1000, 2000, and 3000#), as well as polishing with Al_2O_3 and SiO_2 solutions. Finally, the polished surfaces were etched with a nitric acid alcohol solution (4 wt%) for 10 s before drying.

The single tracks of Zn–3Mg were observed using optical microscopy (OM). The microstructure, tensile fracture surfaces, and corrosive products of the LPBF-fabricated Zn–Mg alloy, with and without annealing, were observed using SEM. The composition of Zn–Mg alloy powders and elemental distribution on the polished surfaces, fracture surfaces, and corroded surfaces of the Zn–Mg alloys were characterized using energy-dispersive X-ray spectroscopy (EDS, FEI Nova nano 430, Netherlands). The phase composition of the LPBF-fabricated Zn–Mg alloys, with and without annealing, was analyzed using X-ray diffraction

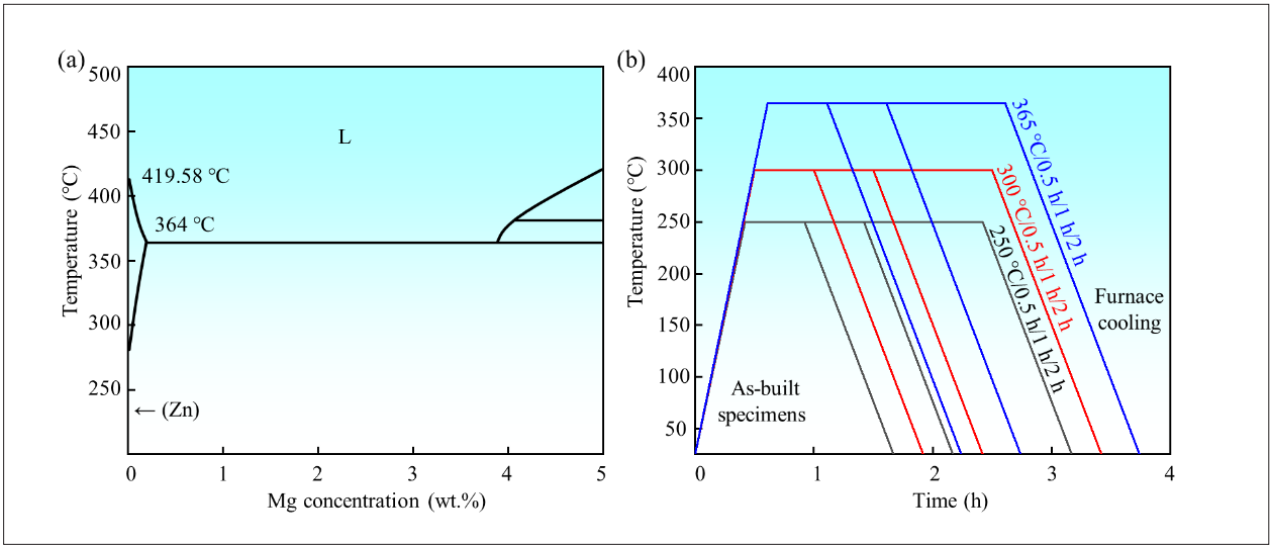

Figure 3. Annealing of the as-built Zn–Mg alloys: (a) Zn–Mg phase diagram and (b) processing curves.

(XRD, Empyrean, Malvern Panalytical, United Kingdom [UK]). Their grain morphology and crystallographic orientation were analyzed using electron backscatter diffraction (EBSD, Symmetry, Oxford Instrument Corp., UK) after electrolytically polished in a solution containing 5 vol% perchloric acid and 95 vol% ethanol.

2.5. Mechanical testing

Tensile tests were conducted on the LPBF-fabricated Zn–Mg alloy using a universal mechanical testing machine (CMT5105, SANS, China) with a rate of 0.1 mm/min, following the ASTM E209-18 standards.[34] Prior to the test, the tensile samples were polished using 180# sandpaper to reduce the influence of surface oxides on dimension accuracy. To ensure reliable results and reduce experimental uncertainties, three samples were tested for each process parameter or annealing condition. The tensile fracture morphology of both as-built and annealed Zn–Mg samples was observed using SEM.

2.6. Immersion test

Immersion testing was conducted in a simulated body fluid (SBF) solution at a temperature of 37°C and a pH value of 7.4, following the ASTM-G31-72 standard.[35] The pH value of the solution was continuously measured throughout the immersion process, while the corrosive surface of the Zn–Mg alloys after 1–4 weeks of immersion was examined using SEM. After a 4-week immersion period, the as-built Zn–Mg samples with different Mg concentrations were extracted from the SBF solution, and any corrosive products were cleaned in order to measure the weight of the samples. The corrosion rates were calculated based on the weight loss values, density, exposed surface area, and soaking time.

3. Results and discussion

3.1. Printability of Zn–Mg alloys via laser powder bed fusion

The printability of Zn–Mg alloys with various Mg concentrations via LPBF was investigated. Figure 4 presents the printability of the representative Zn–Mg alloy with 3 wt% Mg under different process parameters. Figure 4a displays the width variation of the printed Zn–3Mg single tracks across various laser powers (50–90 W) and scanning speeds (400–900 mm/s). The results demonstrated that at the scanning speed of 400 mm/s, the single-track width exhibited the most significant variation, increasing from 102.2 ± 4.02 to 137.67 ± 4.16 μm before decreasing to 113.67 ± 3.79 μm as the laser power increased from 50 to 90 W. At the scanning speed of 900 mm/s, the single-track width also experienced notable changes, increasing from 73.00 ± 3.61 to 85.67 ± 1.53 μm before decreasing to 79.33 ± 2.08 μm. Likewise, the low volume density was insufficient for complete powder melting, leading to the slightest change in the width of the single track. The single-track width demonstrated an initial increase followed by a decrease with increasing laser power. In contrast, the single-track width consistently decreased with the increased scanning speed. This widening could be attributed to elevated laser energy density, which resulted in thermal energy transfer into the surrounding powder, causing partial melting. In cases where incomplete melting occurred to the surrounding powder, agglomeration could occur.[36,37] Excessive energy density can cause material evaporation, disrupting molten pools and resulting in Zn–Mg alloy fabrication failure.

The OM images of the representative Zn–3Mg single tracks are presented in Figure 4b. It could be observed that utilizing a laser power of 50 W and a scanning speed of 800 mm/s, the laser energy density was relatively low, leading to incomplete melting of the Zn–3Mg powder and leaving some unmelted powder within the interior of the single tracks. As the laser power increased to 60 W and the scanning speed decreased to 500 mm/s, the corresponding energy density values gradually increased to 72.73 J/mm^3. There was a significant improvement in the overall continuity as there was almost no visible disconnection (due to incomplete melting) on the surface of the formed Zn–Mg single track. Furthermore, at a higher laser power of 80 W and scanning speed of 600 mm/s, the energy density further increased to 80.81 J/mm^3, which displayed even better continuity without any noticeable disconnection on the surface. However, when utilizing the laser power of 90 W and the scanning speed of 600 mm/s, the energy density increased up to 90.91 J/mm^3, which disrupted the melt pool, leading to a high degree of discontinuity in the single track and resulting in poor quality fabrication.

The relative density of the LPBF-fabricated Zn–3Mg alloy is illustrated in Figure 4c and d. Several defects, such as balling, porosity, cracks, and warpage, were identified within the processing window. For instance, Zn–3Mg cubic samples failed to be fabricated under the laser powers in the range of 50–90 W with the scanning speed value setting at 400 mm/s, and this could be ascribed to the balling or warping phenomenon. Under identical process parameters, Zn–Mg alloy with 5 wt% Mg exhibited higher susceptibility towards balling or warping compared to other compositions. The relative density of the Zn–3Mg alloy increased with increasing laser power or decreasing scanning speed, thereby correlating with augmented energy density. When the energy density was 68.18–80.81 J/mm^3, LPBF could print Zn–3Mg alloy with a high relative density (>97%). However, when the energy density exceeded 90 J/mm^3, balling or warping occurred. Using a laser power of 80 W and a scanning speed of 600 mm/s,

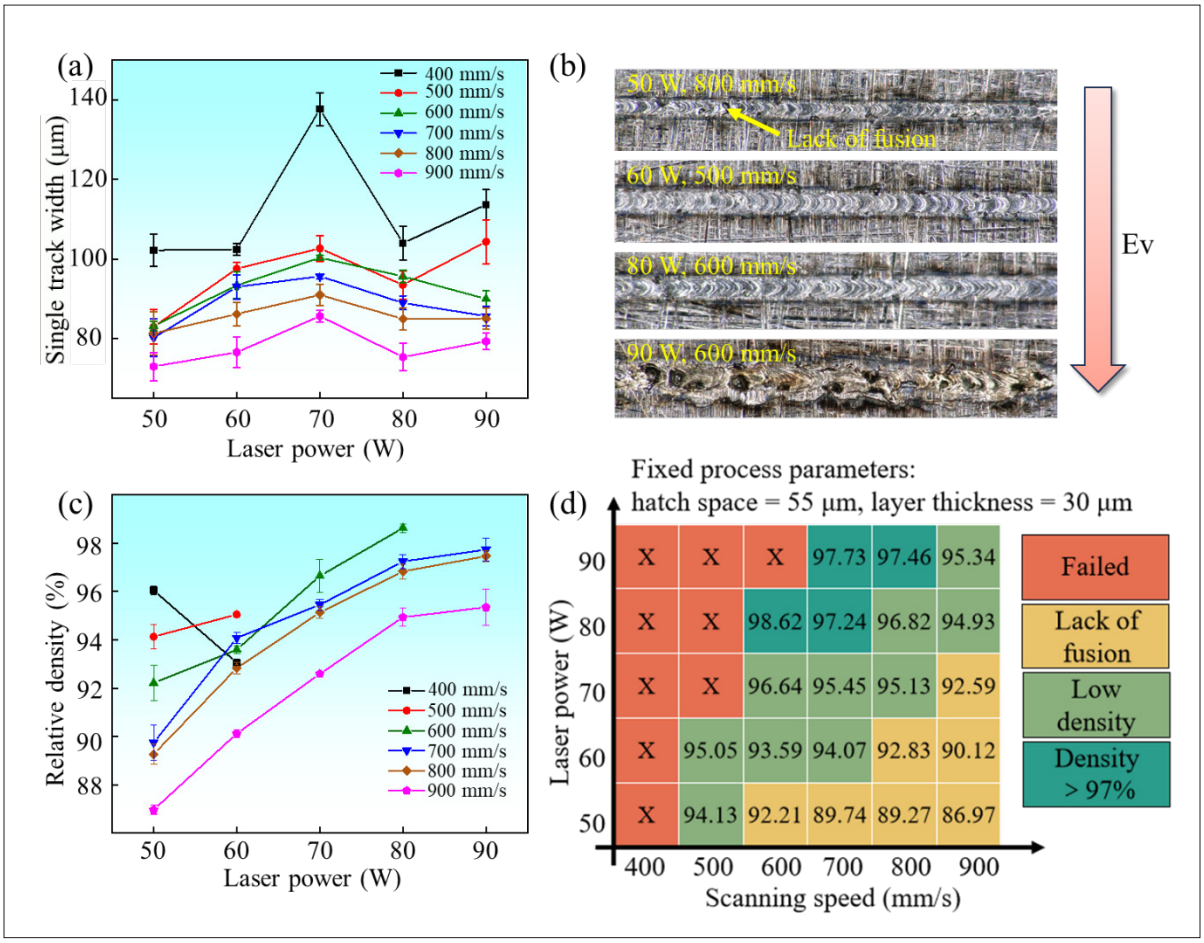

Figure 4. Printability of laser powder bed fusion (LPBF)-fabricated Zn–Mg alloy with 3 wt% Mg: (a) width of single tracks, (b) optical microscopy image of single tracks, (c) relative density variation, and (d) optimized process parameter window. Abbreviation: Ev, volume energy density.

the LPBF-fabricated Zn–Mg alloy exhibited the highest relative density at 98.62%. All the fabricated Zn–Mg alloys achieved optimal densification at the laser power of 80 W and scanning speed at 600–800 mm/s.

3.2. Microstructure of fabricated Zn–Mg alloys

The XRD results of the LPBF-fabricated Zn–Mg alloys with different Mg concentrations are depicted in Figure 5. Initially, the diffraction peaks that corresponded to the hexagonal close-packed crystal structure of α-Zn were observed in the fabricated Zn–Mg alloys at all compositions. Subsequently, no distinct diffraction peaks of Mg_2Zn_{11} were obtained in the Zn–1Mg alloy with a predominant α-Zn phase due to its lower Mg concentration. In contrast, both Mg_2Zn_{11} and $MgZn_2$ phases were identified in the Zn–3Mg and Zn–5Mg alloys, and their intensities increased significantly with increasing Mg concentration. Notably, higher intensity peaks of Mg_2Zn_{11} and $MgZn_2$ were achieved in the Zn–5Mg alloy. Additionally, no peaks indicative of ZnO were observed, signifying the absence of oxidation in the vacuum environment during the LPBF process. From the phase diagram for Zn–Mg alloys, the precipitation of Mg_2Zn_{11} and $MgZn_2$ phases occurred at approximately 364°C.

The morphology and corresponding element distributions of LPBF-fabricated Zn–Mg alloys are presented in Figure 6. In Figure 6a, d, and g, the grain size of Zn–Mg alloys decreased with increasing Mg concentration. The grain sizes were approximately 1–2, 0.5–1, and 0.5 μm for Zn–1Mg, Zn–3Mg, and Zn–5Mg, respectively. The addition of Mg primarily contributed to grain refinement in Zn–1Mg, while eutectic structures became more pronounced in Zn–3Mg (indicated by dark regions). Additionally, irregular polyhedral second-phase structures were significantly present in Zn–5Mg. Elemental composition analysis using EDS illustrated the presence of α-Zn matrix and a second phase in LPBF-fabricated Zn–

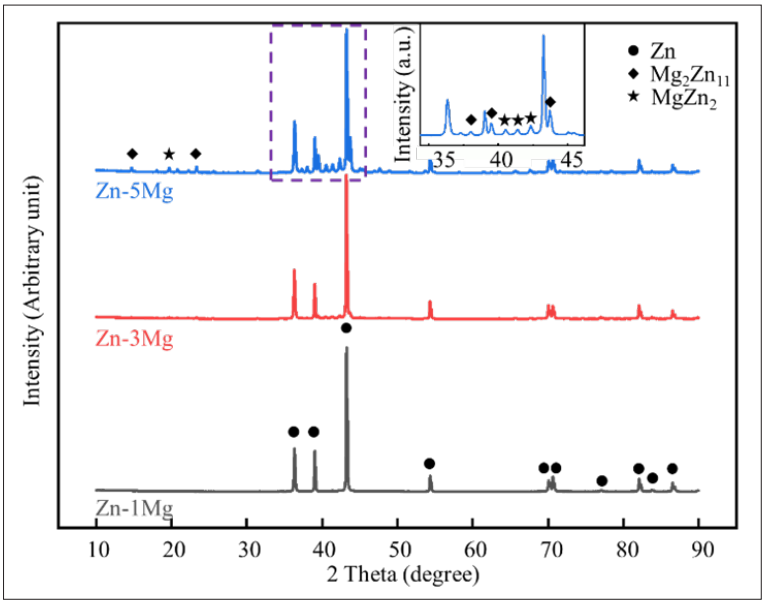

Figure 5. X-ray diffraction (XRD) patterns of laser powder bed fusion (LPBF)-fabricated Zn–Mg alloys with different Mg concentrations.

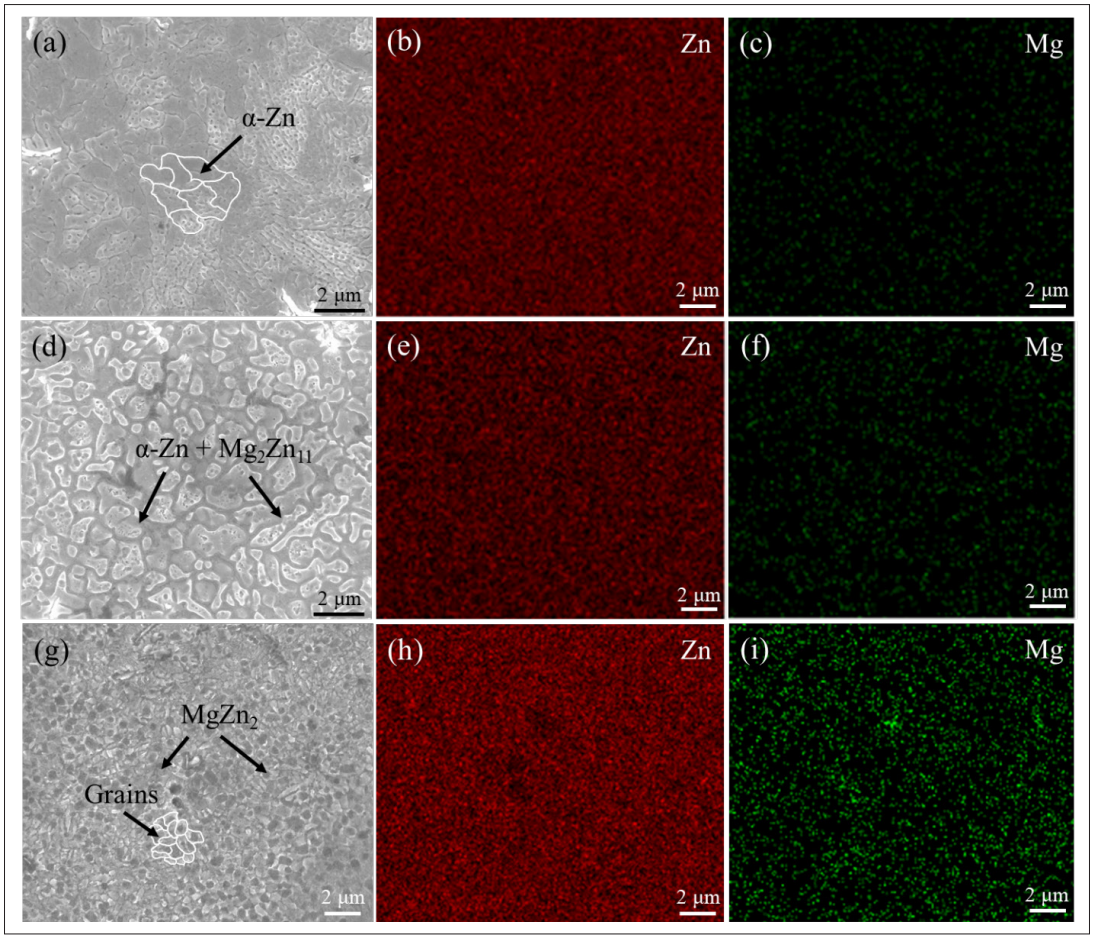

Figure 6. Morphology and element distributions of laser powder bed fusion (LPBF)-fabricated Zn–Mg alloys: (a–c) Zn–1Mg, (d–f) Zn–3Mg, and (g–i) Zn–5Mg.

Mg alloys (Table 2). The Mg concentration within the α-Zn matrix for Zn–1Mg, Zn–3Mg, and Zn–5Mg was 0.74, 1.15, and 3.20 wt%, respectively. With an increase in Mg concentration, the concentration of dissolved Mg within the α-Zn matrix also increases. Furthermore, a comparison between the Mg concentration at grain boundaries and within the matrix for the same compositions demonstrated the enrichment of Mg at the grain boundaries of the α-Zn matrix. The polyhedral structure exhibited by the black grains (observed in the SEM images) suggests that they corresponded to the $MgZn_2$ phase.

3.3. Degradation characteristics of fabricated Zn–Mg alloys

The LPBF-fabricated Zn–Mg alloys, which exhibited the highest relative density, were assessed for their degradation properties. Figure 7 depicts the *in vitro* immersion corrosion behaviors of the fabricated Zn–Mg alloys with varying Mg concentrations. The pH variation curves of the SBF solution after immersing the Zn–Mg alloys for 28 days are depicted in Figure 7a. The pH values of the three alloys rapidly increased within the initial 10 days of immersion, reaching a relatively stable state at day 14. The increase in pH can primarily be ascribed to the release of OH^- ions during the immersion process:[38]

$$M + 2H_2O \rightarrow M^{2+} + H_2 + 2OH^- \quad (2)$$

where M represents Zn or Mg. Among them, the fabricated Zn–1Mg alloy exhibited a slightly higher pH compared to that of the Zn–3Mg and Zn–5Mg alloys, suggesting a higher corrosion rate for Zn–1Mg than for Zn–3Mg and Zn–5Mg. Figure 7b presents the ion concentrations of the alloys after immersing the alloys for 28 days in the SBF solution. The concentration of Zn^{2+} remained consistent across all three alloys at approximately 30 mg/L. Conversely, the concentration of Mg^{2+} decreased from 89.72 to 38.01 mg/L as the Mg concentration ranged from 1 to 5 wt%. Figure 7c illustrates the corrosion rates of Zn–1Mg, Zn–3Mg, and Zn–5Mg alloys during the immersion corrosion process, which are calculated to be 0.126, 0.113, and 0.090 mm/year, respectively. These results indicated that increasing the Mg concentration would reduce the corrosion rate of Zn–Mg alloys.

Table 2. Mg concentration (wt%) of laser powder bed fusion (LPBF)-fabricated Zn–Mg alloys measured through energy-dispersive X-ray spectroscopy (EDS)

Position	Mg concentration (wt%)		
	Zn–1Mg	Zn–3Mg	Zn–5Mg
Grain	0.78 ± 0.05	1.15 ± 0.09	3.20 ± 0.09
Grain boundary	1.74 ± 0.12	4.74 ± 0.22	5.45 ± 0.89

The morphologies of the surfaces of the LPBF-fabricated Zn–1Mg, Zn–3Mg, and Zn–5Mg alloys (immersed in the SBF solution for 14 days) are presented in Figure 8a, e, and i, respectively. Generally, no visible cracks or pores were observed on the surfaces of LPBF-fabricated Zn–Mg samples, indicating minimal corrosion. The standard potential of Zn–Mg intermetallic compounds is similar to pure Zn,[26,39] indicating negligible galvanic corrosion. After 14 days, the three alloys exhibited uniformly distributed white spherical corrosive products (~1 μm). Among them, the surface of Zn–1Mg displayed the most extensive corrosive product coverage (60–70% of the total visual field area), with some aggregation and small cracks appearing in the precipitates. The surface of Zn–3Mg displayed slightly fewer corrosive products compared to Zn–1Mg; however, there was a slight product aggregation without observable cracks in the precipitates. In contrast, only scattered corrosion products were observed on the surface of Zn–5Mg.

The morphologies of the fabricated Zn–1Mg, Zn–3Mg, and Zn–3Mg alloy surfaces after 28 days of immersion are depicted in Figure 8b, f, and j, respectively. A significant increase in both the quantity and size of corrosive products on the surfaces of the three alloys was observed, with complete coverage of the visual field area. Specifically, the size of the corrosive products on the Zn–1Mg surface grew to approximately 2 μm, accompanied by wider cracks within the precipitates that spanned across the entire surface. Medium-sized areas displayed detachment within these precipitates. The Zn–1Mg matrix exhibited a smooth and flat surface, indicating the prevention of further corrosion within the film.[40] An enhanced aggregation of corrosive products with dispersed tiny cracks was observed on the surface of Zn–3Mg. Although noticeable growth and aggregation occurred on the surface of Zn–5Mg, it was lower compared to that observed for Zn–1Mg. Throughout the entire immersion testing, Zn–1Mg exhibited a significantly higher abundance of surface corrosive products compared to Zn–3Mg and Zn–5Mg. Moreover, Zn–1Mg displayed an accelerated corrosion rate, resulting in the generation of a greater quantity of corrosive products within the same time frame. EDS analysis performed on the corrosive products from the Zn–Mg alloys indicated the presence of Zn, Ca, P, Cl, and O. The predominant constituents identified for the corrosive products in a chloride solution were zinc oxide, zinc hydroxycarbonate, and zinc hydroxyphosphate.[34,41]

The corrosion resistance of LPBF-fabricated Zn–Mg alloy improved with increasing Mg concentration, and this could be attributed to the formation of a Mg-rich

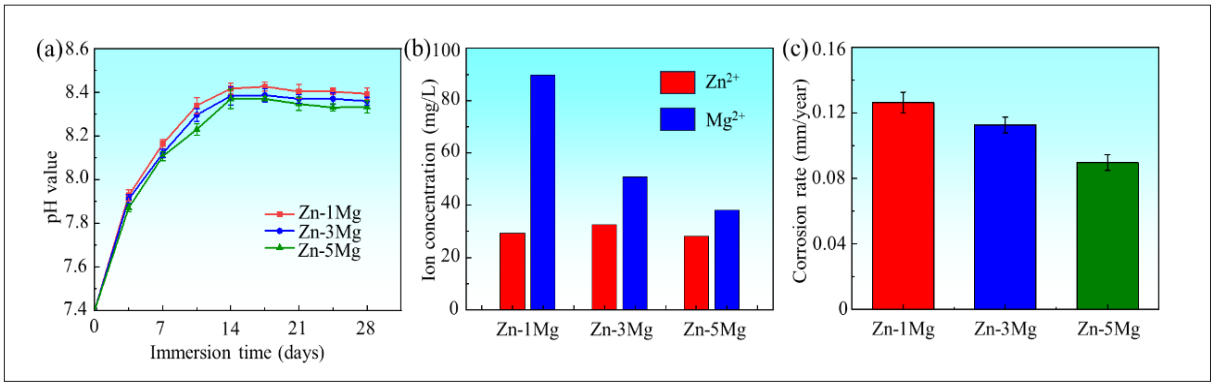

Figure 7. Corrosion behavior of laser powder bed fusion (LPBF)-fabricated Zn–Mg alloys with different Mg concentrations: (a) pH variation curves of simulated body fluid (SBF) with immersion time, (b) ion concentration, and (c) corrosion rates.

oxide layer at a higher band gap with a lower conductivity than ZnO. This Mg-rich oxide layer effectively reduces the cathodic reaction between Zn and Mg at the corrosion stage.[42,43] With the increase in Mg concentration in the Zn–Mg alloys, the surface of Zn–Mg alloy exhibited an elevated MgO concentration, which inhibited the cathodic reaction and decelerated the degradation process of Zn–3Mg and Zn–5Mg alloys. The corrosion of the Mg-rich phases sufficiently lowers the surface pH, thereby facilitating the general precipitation of zinc chloride hydroxide monohydrate.[41] Due to its modification by Mg, zinc chloride hydroxide monohydrate exhibits reduced solubility compared to that deposits on the surface of the Zn matrix. Compared to LPBF-fabricated Zn–1Mg, the presence of higher concentrations of Mg_2Zn_{11} and $MgZn_2$ phases on the surface in Zn–3Mg and Zn–5Mg results in increased zinc chloride hydroxide monohydrate precipitation, thereby retarding the corrosion reaction. Zinc chloride hydroxide monohydrate formation can be described as follows:

$$5ZnO + 2Cl^- + 6H_2O \rightarrow Zn_5(OH)_8Cl_2H_2O + 2OH^- \quad (3)$$

To promote the formation of zinc chloride hydroxide monohydrate on the surface of the alloys, it is imperative to neutralize or remove OH^-. The formation of magnesium hydroxycarbonate as a corrosive product can be described as follows:

$$2Mg^{2+} + 2OH^- + 6\ CO_2^{2-} \rightarrow Mg_2(OH)_2CO_3. \quad (4)$$

$Mg_2(OH)_2CO_3$ is characterized as an electrochemically inert material that effectively removes OH^- and lowers the surface pH, facilitating general precipitation of zinc chloride hydroxide monohydrate.[41] The presence of $Mg_2(OH)_2CO_3$ facilitates zinc chloride hydroxide monohydrate formation on the Mg-rich phases by sequestering carbonate, thus impeding its transformation into Zn-rich minerals. This resulting carbon-based corrosive product exhibits limited solubility and acts as a protective film.[44] Finally, incorporating Mg promoted grain refinement in LPBF-fabricated Zn–Mg alloys, leading to increased grain boundary density. Smaller grain sizes corresponded to lower corrosion currents and improved corrosion resistance for Zn–3Mg and Zn–5Mg.[45] The LPBF-fabricated Zn–3Mg and Zn–5Mg alloys exhibited enhanced Mg^{2+} ion release during degradation, thereby promoting the precipitation of alkaline magnesium carbonate and decelerating the degradation rate.

3.4. Annealing effect on laser powder bed fusion-fabricated Zn–Mg alloy

Since the LPBF-fabricated Zn–Mg alloy with 1 wt% Mg under the laser power of 80 W and scanning speed of 600 mm/s exhibited a degradation rate similar to that of ideal biodegradable metal implants (0.2–0.3 mm/year), annealing was applied to the fabricated Zn–1Mg alloy to identify an effective approach to modify the microstructure, degradation characteristics, and mechanical properties of Zn–Mg alloys.

The XRD pattern, microstructural features, and element distribution of the as-built alloy after annealing are presented in Figure 9. Figure 9a illustrates the XRD pattern of the alloy annealed at 300°C for 0.5 h. It was observed that there were no significant changes in the intensities of the diffraction peaks corresponding to Mg_2Zn_{11} and $MgZn_2$ after annealing. The slight variations in peak intensity suggested that annealing at 300°C did not induce significant modifications in the phases of the as-built alloy. As presented in Figure 9b, the grain size within the alloy annealed at 250°C for 0.5 h was observed to be 2–4 μm, which was larger than that of the as-built alloy

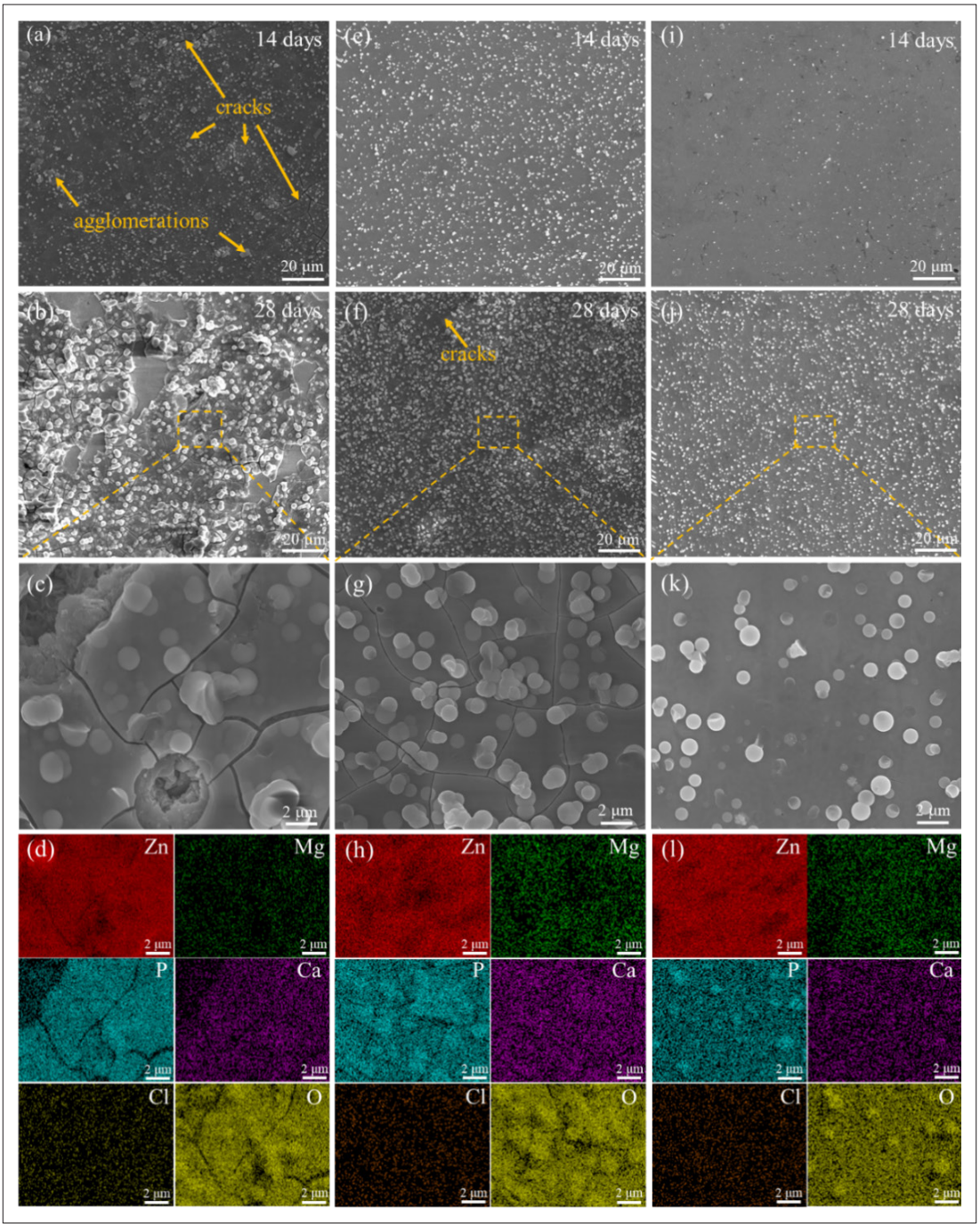

Figure 8. Morphology and element distribution of laser powder bed fusion (LPBF)-fabricated Zn–Mg alloys after immersion in simulated body fluid (SBF) solution for 14 and 28 days: (a–d) Zn–1Mg, (e–h) Zn–3Mg, and (i–l) Zn–5Mg.

(~1–2 μm). EDS analysis of the annealed alloy is displayed in Figure 9c, revealing a continued enrichment of Mg at the grain boundaries. In Figure 9d, the grain size of the Zn–Mg alloy annealed at 300°C for 0.5 h was reduced to approximately 1 μm, compared to that of alloys annealed at 250°C. Elemental analysis of both grains and grain boundaries of the alloy annealed at 300°C, as displayed in Figure 9e, indicated that the Mg concentration in the α-Zn matrix and at the grain boundaries was 0.21% and 3.17%, respectively. At an annealing temperature of 300°C,

a significant decrease observed in the Mg concentration was observed within the α-Zn matrix compared to that of the as-built alloy. Meanwhile, more accumulation occurred along the grain boundaries, which aligned with the observations at 250°C annealing temperature. Figure 9f illustrates numerous pores present within the Zn–Mg alloy annealed at 365°C, of which could be a major factor contributing to the substantial decline of the alloy's mechanical properties.

To investigate the effect of annealing on the electrochemical properties of the LPBF-fabricated Zn–Mg alloy, the electrochemical properties of Zn–1Mg alloy were evaluated and the polarization curves were presented in Figure 10. The corrosion potentials (E_{corr}) for both as-built and annealed Zn–1Mg alloy samples were determined to be −1.115 ± 0.008 and −1.116 ± 0.003 V, respectively. The corrosion current densities (I_{corr}) of the as-built Zn–1Mg alloy were calculated using the extrapolation method. Notably, an inflection point was observed in the anodic part of the polarization curve for the annealed sample (as indicated by a black arrow), indicating the occurrence of passivation and resulting in a sudden increase in the current density at this point. Hence, the cathodic polarization region was used to calculate the I_{corr} of the annealed sample. Consequently, the corrosion current densities were calculated to be 9.618 ± 0.345 and 14.091 ± 0.903 μA/cm^2 for the as-built and annealed Zn–1Mg samples, respectively. The degradation rate (R_d) can be calculated as follows:

$$R_d = 3.27 \times 10^{-3} \frac{I_{corr}}{\rho} me \quad (5)$$

where ρ and m_e are the density (g/cm^3) of Zn–1Mg alloy and its equivalent metal mass, respectively. For Zn-1Mg, ρ was determined to be 6.9521 g/cm^3, and m_e was calculated as 32.4847. The degradation rate of the as-built and annealed Zn–1Mg alloy was evaluated to be 0.147 and 0.215 mm/year, respectively, indicating that annealing accelerated the degradation of LPBF-fabricated Zn–Mg alloy.

After annealing, the grain size of Zn–Mg alloy increased, leading to a decrease in the grain boundary density and an increase in the corrosion current, thereby accelerating the degradation rate. Simultaneously, the finer grain size facilitated the formation of a continuous oxide layer on the surface of Zn–Mg alloy, effectively inhibiting further inward degradation reactions. However, annealing also promoted Mg enrichment at grain boundaries and increased the Mg_2Zn_{11} and $MgZn_2$ phases. These phases

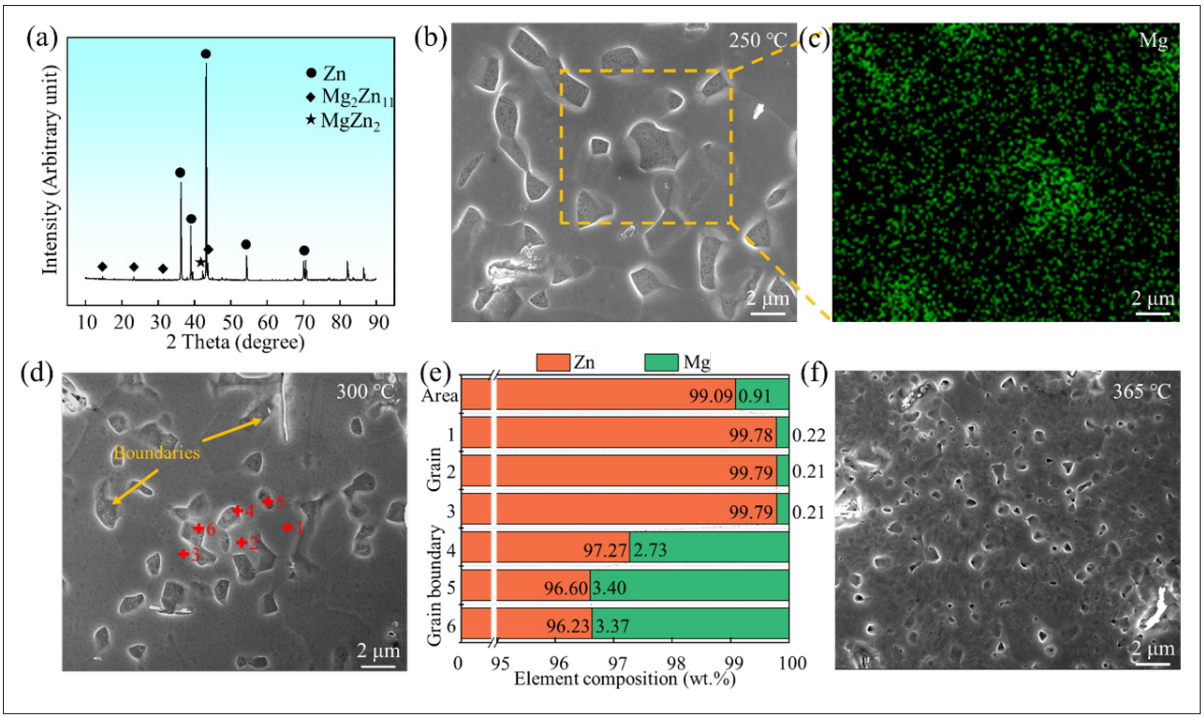

Figure 9. Annealing effect on laser powder bed fusion (LPBF)-fabricated Zn–Mg alloy: (a) X-ray diffraction (XRD) pattern of the annealed Zn–Mg alloy; morphology of the LPBF-fabricated Zn–Mg alloy at different annealing temperatures: (b) 250°C, (d) 300°C, and (f) 365°C; element distribution of the LPBF-fabricated Zn–Mg alloy: (c) Mg distribution at 250°C annealing temperature, and (e) Zn and Mg concentrations at the point in 300°C annealing temperature.

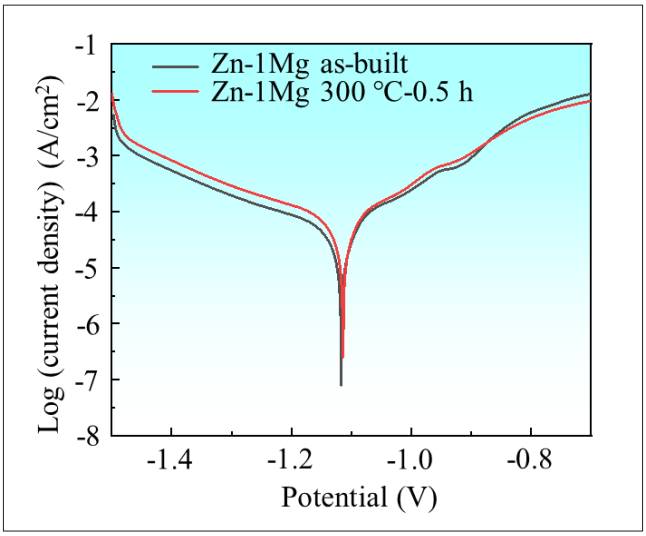

Figure 10. Polarization curves of the as-built and annealed Zn–1Mg alloys in simulated body fluid (SBF) solution.

form primary cells with Zn, acting as the anode for electrochemical corrosion due to their lower standard potential compared to that of Zn. Consequently, as both the size and number of Mg_2Zn_{11} and $MgZn_2$ phases increased, the extent of electrochemical corrosion and degradation rate in the annealed Zn–Mg alloy also improved. Although the as-built Zn–3Mg and Zn–5Mg alloys had finer grain sizes than Zn–1Mg alloy, they exhibited higher concentrations of Mg_2Zn_{11} and $MgZn_2$ phases, resulting in a lower degradation rate compared to that observed in Zn–1Mg. This suggests that both grain sizes and crystal phases regulate the degradation rate of LPBF-fabricated Zn–Mg alloys, with grain size as the more prominent factor.

The microstructure of the LPBF-fabricated Zn–1Mg alloy, with or without annealing, was evaluated using EBSD. Figure 11a, b, c, g, and i corresponds to the as-built Zn–1Mg alloy, while Figure 11d, e, f, h, and j represents the Zn–1Mg alloy annealed at 300°C for 0.5 h. In Figure 11a and d, brighter regions in the bond contrast maps indicate a well-ordered crystal lattice structure, whereas darker regions represent the presence of defects, strains, or orientation differences. The crystal lattice structure of the annealed Zn–Mg alloy exhibited improvements compared to the as-built alloy. Moreover, annealing treatment reduced low-angle grain boundaries in the as-built alloy while increasing high-angle grain boundaries, thereby affecting atomic bonding, diffusion rate, and grain nucleation. Figure 11b and e presents bimodal grain structures composed of fine and large grains in the as-built alloy. Recrystallized microstructure maps are displayed in Figure 11c and f. Blue, yellow, and red regions represent recrystallized, recovered, and deformed grains, respectively. After annealing, the size of recovery grains increased in the Zn–Mg alloy. The grain size maps in Figure 11g and h demonstrated that annealing eliminated fine grains in the annealed Zn–Mg alloy, leading to an increase in the average grain size, induction of recrystallization, and transformation of as-built alloy grains towards equiaxed morphology. Annealing resulted in larger grain size for the Zn–Mg alloy, reducing the area occupied by grain boundaries, minimizing slip hindrance, and consequently decreasing mechanical strength. Pole figures in Figure 11i and j indicated that the maximum intensity of multiples of uniform density (MUD) for the as-built alloy was 2.74 MUD, while the annealed Zn–Mg alloy reached 4.58 MUD. Annealing also enhanced the texture of the as-built Zn–Mg alloy with a more preferred {0 0 0 1} orientation.

The annealing process parameters, such as temperature and holding time, significantly influenced the mechanical properties of the LPBF-fabricated Zn–1Mg alloy (Figure 12a and b). In Figure 12a, it was evident that all annealing conditions resulted in an improvement in the elongation of the LPBF-fabricated Zn–1Mg alloy. The mechanical properties of the as-built alloy reached a maximum tensile strength of 254.92 ± 7.31 MPa with an extremely low elongation of 0.55 ± 0.12%. After annealing at 300°C for 0.5 h, both tensile strength and elongation were 170.93 ± 3.01 MPa and 8.43 ± 0.33%, respectively. Compared to the as-built alloy, the tensile strength decreased to 67% of its original value while elongation increased significantly by 14.3 times when subjected to this temperature.

Under the annealing temperature of 250°C, both tensile strength and elongation exhibited an increasing trend followed by a decrease with increasing holding time. When

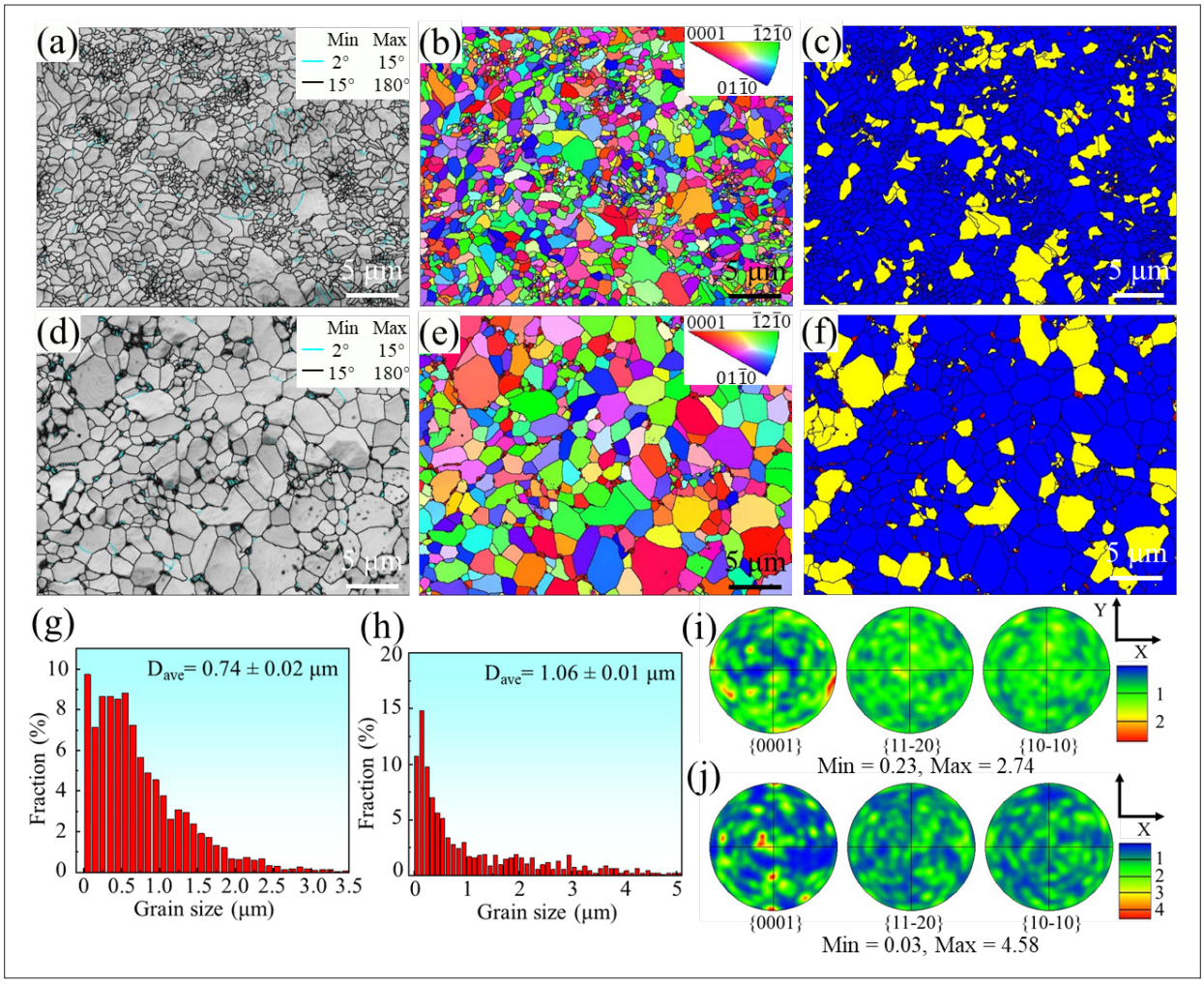

Figure 11. Electron backscatter diffraction (EBSD) analysis of the laser powder bed fusion (LPBF)-fabricated Zn–Mg alloy with and without annealing (300°C for 0.5 h): (a–c) bond contrast map, grain size map, and recrystallized microstructure map of the as-built alloy, respectively; (d–f) bond contrast map, grain size map, and recrystallized microstructure map of the annealed alloy, respectively; (g and h) the grain size distribution of the as-built and annealed alloy, respectively; and (i and j) pole figure of the as-built and annealed alloy, respectively.

the holding time was 1 h, tensile strength and elongation were 175.88 ± 3.24 MPa and 6.53 ± 0.10%, respectively. At 365°C, there was no significant difference observed in the tensile strength and elongation of the alloy after 0.5, 1, and 2 h of holding; they remained consistently lower at approximately 90 MPa and 0.8%. When the temperature exceeded the optimal range, the influence of holding time on mechanical properties was relatively minimal, resulting in a sustained lower level. Furthermore, it was found that all annealing conditions generally resulted in reduced tensile strength of the annealed alloy compared to the as-built alloy. The comparative analysis of tensile performance for LPBF-fabricated Zn–Mg is presented in Figure 12c. Notably, the elongation of the Zn–Mg alloy after annealing exceeded those of the LPBF-fabricated Zn–Mg alloy, and the annealed Zn–Mg alloy exhibited higher tensile strength than most LPBF-fabricated counterparts. These findings indicated that annealing can effectively improve the overall mechanical properties of as-built Zn–Mg alloys.

The tensile fractured morphology of the annealed Zn–1Mg alloy was characterized using SEM to further investigate the influence of annealing (Figure 13). In Figure 13a, the fractured surface of the Zn–Mg alloy annealed at 250°C exhibited distinct features, such as cleavage steps and river-like patterns, accompanied by numerous smooth cleavage planes of 20–40 μm in length, indicating pronounced brittleness and a quasi-cleavage fracture mode. In Figure 13b, the fractured surface of the Zn–Mg alloy annealed at 300°C displayed smaller dimensions for

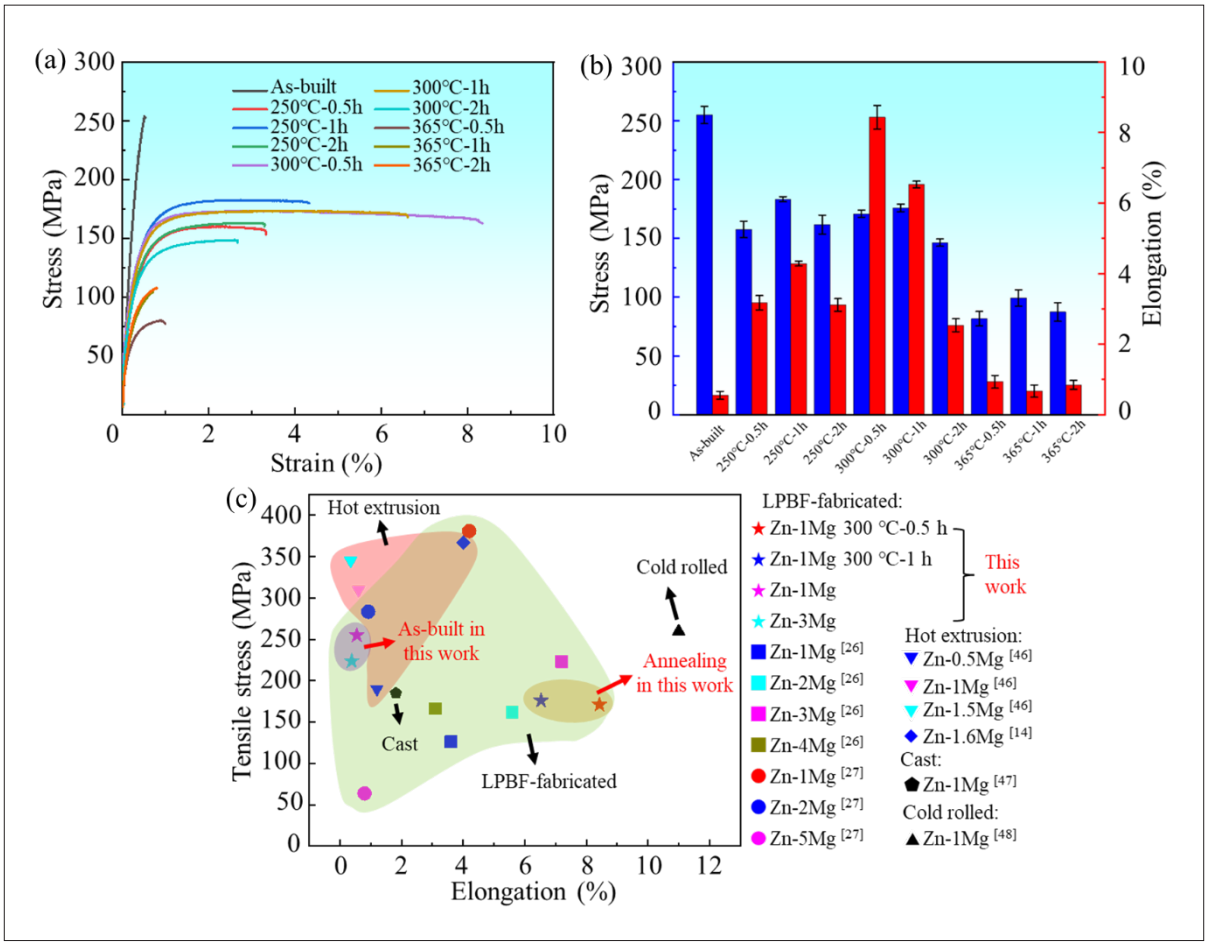

Figure 12. Mechanical properties of the laser powder bed fusion (LPBF)-fabricated Zn–Mg alloy after annealing at different parameters: (a) stress–strain responses; (b) tensile strength and elongation; and (c) a comparison of tensile properties of Zn–Mg alloys.[14,26,27,46–48]

the cleavage planes (~5 μm) compared to those observed in the Zn–Mg alloy annealed at 250°C. In Figure 13c, the cleavage plane dimensions of the Zn–Mg alloy annealed at 365°C (~10 μm) fell between those observed in the Zn–Mg alloys annealed at both 250 and 300°C. As observed in Figure 13, annealing of the Zn–1Mg alloy exhibited no evident signs of plastic deformation but displayed cleavage fracture characteristics, such as river patterns, on its morphology.

After annealing at 300°C for 0.5 h, the ultimate tensile strength of the Zn–1Mg alloy decreased by 32.9%, while the elongation increased by a factor of 14.3. It could also be observed from Figure 11b and e that the as-built alloy exhibited bimodal grains with numerous dislocations between grains of different sizes, thereby enabling mechanical reinforcement mechanisms, such as grain boundary reinforcement and dislocation reinforcement, during tensile deformation and resulting in higher tensile strength of the as-built alloy. However, after annealing, the average grain size of Zn–1Mg alloy increased from 0.74 to 1.06 μm, leading to predominantly equiaxed grains in the annealed Zn–Mg alloy. The increase in grain size resulted in a decrease in grain boundaries within the annealed Zn–Mg alloy and subsequently reduced dislocation movements generated during tensile deformation, ultimately decreasing the tensile strength but increasing the plasticity of the Zn–Mg alloy. From the EBSD characterization (Figure 11a and d), fewer low-angle grain boundaries were observed within the annealed alloy compared to those found within the as-built alloy, further validating that annealing effectively reduced dislocation density in the Zn–Mg alloy. The reduction in dislocations leads to a decrease in slip systems available for deformation during the tensile process, decreasing the tensile strength but increasing the plasticity of the annealed Zn–Mg alloy.

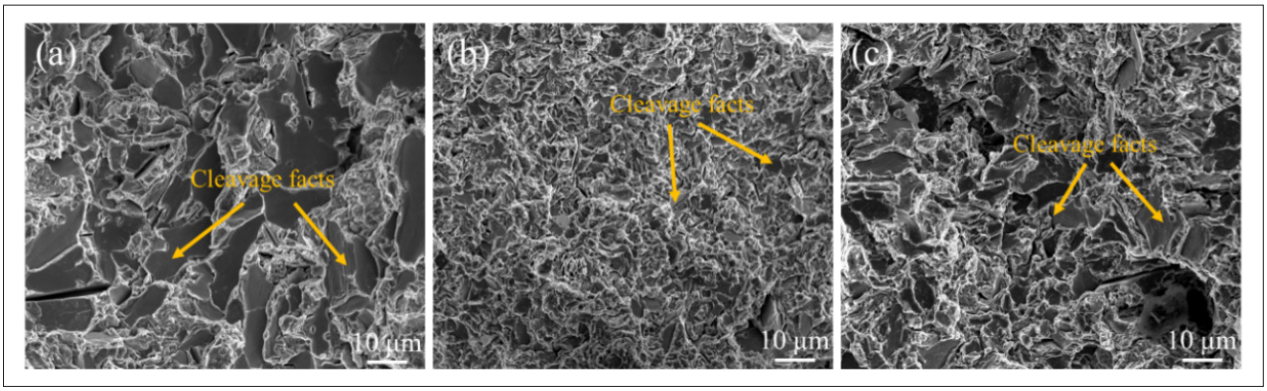

Figure 13. Fractured morphologies of the laser powder bed fusion (LPBF)-fabricated Zn–Mg alloy annealed at different temperatures: (a) 250°C, (b) 300°C, and (c) 365°C.

4. Conclusion

This work investigated the influence of Mg concentration on the printability, microstructure, mechanical properties, and degradation behavior of LPBF-fabricated Zn–Mg alloys. Furthermore, a viable annealing post-processing route was proposed to modify the microstructure of the fabricated Zn–Mg alloy and improve its ductility. The primary findings of this work are summarized as follows.

(i) The LPBF-fabricated Zn–Mg alloy achieved the highest relative density (98.62%) under the laser power of 80 W and scanning speed of 600 mm/s. Excessive energy density (>90 J/mm^3) led to balling, cracks, and warpage in the Zn–Mg alloy, resulting in printing failure. Increasing Mg concentration from 1 to 5 wt% refined the grains of the Zn–Mg alloy with enriched Mg at grain boundaries and increased the concentrations of Mg_2Zn_{11} and $MgZn_2$.

(ii) Compared to Zn–3Mg and Zn–5Mg alloys (0.113 and 0.090 mm/year, respectively), the LPBF-fabricated Zn–1Mg alloy exhibited the highest degradation rate at 0.126 mm/year. The spherical corrosive products mainly consisted of zinc oxides and basic zinc carbonate. An increase in Mg concentration enhanced corrosion resistance in the fabricated Zn–Mg alloys, resulting in slower degradation rates.

(iii) Annealing resulted in increased average grain size, transformation to equiaxed grains, and an increased in high-angle grain boundaries, as well as enhanced enrichment of Mg at grain boundaries for the as-built Zn–Mg alloy containing 1 wt% Mg. Annealing at a temperature of 300°C for 0.5 h caused a decrease in ultimate tensile strength by 32.9% from 254.92 to 170.93 MPa, but increased elongation by 14.3 times from 0.55% to 8.43%. This could be attributed to the increase in grain size and the abundance of α-Zn and Mg_2Zn_{11} phases, thereby reducing slip hindrance while simultaneously promoting the formation of high-angle grain boundaries.

Acknowledgments

None.

Funding

This research was supported by the Fundamental Research Funds for the Central Universities (2023ZYGXZR061), the National Natural Science Foundation of China (52305358), Guangdong Basic and Applied Basic Research Foundation (2021A1515110142, 2022A1515010304), Young Elite Scientists Sponsorship Program by CAST (2023QNRC001), and the Young Talent Support Project of Guangzhou (QT-2023-001).

Conflict of interest

The authors declare no conflicts of interest.

Author contributions

Conceptualization: Changjun Han, Jinmiao Huang, Guocai Chen

Formal analysis: Changjun Han, Jinmiao Huang, Zhi Dong

Investigation: Changjun Han, Jinmiao Huang, Zhi Dong

Methodology: Jinmiao Huang, Xiangling Ye, Junqing Gao, Kuangyang Yang, Guocai Chen

Writing – original draft: Changjun Han, Jinmiao Huang, Zhi Dong

Writing – review & editing: Boxun Liu, Yongqiang Yang, Kuangyang Yang, Guocai Chen

Ethics approval and consent to participate

Not applicable.

Consent for publication

Not applicable.

Availability of data

Not applicable.

References

1. Zhao D, Yu K, Sun T, et al. Material–structure–function integrated additive manufacturing of degradable metallic bone implants for load-bearing applications. *Adv Funct Mater*. 2023;33(16):2213128. doi: 10.1002/adfm.202213128
2. Li H, Wang P, Lin G, Huang J. The role of rare earth elements in biodegradable metals: a review. *Acta Biomater*. 2021;129: 33-42. doi: 10.1016/j.actbio.2021.05.014
3. Shuai C, Zhong S, Shuai Y, Yang W, Peng S, He C. Accelerated anode and cathode reaction due to direct electron uptake and consumption by manganese dioxide and titanium dioxide composite cathode in degradation of iron composite. *J Colloid Interface Sci*. 2023;632(Pt A):95-107. doi: 10.1016/j.jcis.2022.11.055
4. Ling C, Li Q, Zhang Z, et al. Influence of heat treatment on microstructure, mechanical and corrosion behavior of WE43 alloy fabricated by laser-beam powder bed fusion. *Int J Extreme Manuf*. 2023;6(1):015001. doi: 10.1088/2631-7990/acfad5
5. Yang Y, Ling C, Li Y, et al. Microstructure development and biodegradation behavior of additively manufactured Mg-Zn-Gd alloy with LPSO structure. *J Mater Sci Technol*. 2023;144:1-14. doi: 10.1016/j.jmst.2022.09.059
6. Zhou Y, Wang J, Yang Y, et al. Laser additive manufacturing of zinc targeting for biomedical application. *Int J Bioprint*. 2022;8(1):501. doi: 10.18063/ijb.v8i1.501
7. Kabir H, Munir K, Wen C, Li Y. Recent research and progress of biodegradable zinc alloys and composites for biomedical applications: biomechanical and biocorrosion perspectives. *Bioact Mater*. 2021;6(3):836-879. doi: 10.1016/j.bioactmat.2020.09.013
8. Xiao C, Wang L, Ren Y, et al. Indirectly extruded biodegradable Zn-0.05 wt% Mg alloy with improved strength and ductility: in vitro and in vivo studies. *J Mater Sci Technol*. 2018;34(9):1618-1627. doi: 10.1016/j.jmst.2018.01.006
9. Zhang Y, Yan Y, Xu X, et al. Investigation on the microstructure, mechanical properties, *in vitro* degradation behavior and biocompatibility of newly developed Zn-0.8% Li-(Mg, Ag) alloys for guided bone regeneration. *Mater Sci Eng C*. 2019;99:1021-1034. doi: 10.1016/j.msec.2019.01.120
10. Yang H, Jia B, Zhang Z, et al. Alloying design of biodegradable zinc as promising bone implants for load-bearing applications. *Nat Commun*. 2020;11(1):401. doi: 10.1038/s41467-019-14153-7
11. Su Y, Cockerill I, Wang Y, et al. Zinc-based biomaterials for regeneration and therapy. *Trends Biotechnol*. 2019;37(4): 428-441. doi: 10.1016/j.tibtech.2018.10.009
12. Ran Z, Wang Y, Li J, et al. 3D-printed biodegradable magnesium alloy scaffolds with zoledronic acid-loaded ceramic composite coating promote osteoporotic bone defect repair. *Int J Bioprint*. 2023;9(5):769. doi: 10.18063/ijb.769
13. Venezuela J, Dargusch MS. The influence of alloying and fabrication techniques on the mechanical properties, biodegradability and biocompatibility of zinc: a comprehensive review. *Acta Biomater*. 2019;87:1-40. doi: 10.1016/j.actbio.2019.01.035
14. Kubásek J, Vojtěch D, Jablonská E, Pospíšilová I, Lipov J, Ruml T. Structure, mechanical characteristics and *in vitro* degradation, cytotoxicity, genotoxicity and mutagenicity of novel biodegradable Zn–Mg alloys. *Mat Sci Eng C-Mater*. 2016;58:24-35. doi: 10.1016/j.msec.2015.08.015
15. Kubásek J, Vojtěch D, Pospíšilová I, Michalcová A, Maixner J. Microstructure and mechanical properties of the micrograined hypoeutectic Zn–Mg alloy. *Int J Min Met Mater*. 2016;23:1167-1176. doi: 10.1007/s12613-016-1336-7
16. Dong Z, Han C, Zhao Y, et al. Role of heterogenous microstructure and deformation behavior in achieving superior strength-ductility synergy in zinc fabricated via laser powder bed fusion. *Int J Extreme Manuf*. 2024;6(4):045003 do: 10.1088/2631-7990/ad3929
17. Shuai C, Li D, Yao X, Li X, Gao C. Additive manufacturing of promising heterostructure for biomedical applications. *Int J Extreme Manuf*. 2023;5:032012. doi: 10.1088/2631-7990/acded2
18. Zhao D, Han C, Peng B, et al. Corrosion fatigue behavior and anti-fatigue mechanisms of an additively manufactured biodegradable zinc-magnesium gyroid scaffold. *Acta Biomater*. 2022;153:614-629. doi: 10.1016/j.actbio.2022.09.047
19. Zhou K, Han C. *Metal Powder-Based Additive Manufacturing*. John Wiley & Sons; 2023. doi: 10.1002/9783527822249.ch1
20. Bandyopadhyay A, Ciliveri S, Guariento S, Zuckschwerdt N, Hogg WW. Fatigue behavior of additively manufactured Ti3Al2V alloy. *Mater Sci Addit Manuf*. 2023;2(3): 1705. doi: 10.36922/msam.1705

21. Qin Y, Wen P, Guo H, et al. Additive manufacturing of biodegradable metals: current research status and future perspectives. *Acta Biomater*. 2019;98:3-22. doi: 10.1016/j.actbio.2019.04.046

22. Gao C, Li C, Peng S, Shuai C. Spiral-eutectic-reinforced biodegradable Zn–Mg–Ag alloy prepared via selective laser melting. *Chin J Mech Eng Addit Manuf Fron*. 2022;1(2):100022. doi: 10.1016/j.cjmeam.2022.100022

23. Wang C, Hu Y, Zhong C, Lan C, Li W, Wang X. Microstructural evolution and mechanical properties of pure Zn fabricated by selective laser melting. *Mat Sci Eng: A*. 2022;846:143276. doi: 10.1016/j.msea.2022.143276

24. Liu J, Wen P. Metal vaporization and its influence during laser powder bed fusion process. *Mater Des*. 2022;215:110505. doi: 10.1016/j.matdes.2022.110505

25. Ning J, Ma Z, Zhang L, Wang D, Na S. Effects of magnesium on microstructure, properties and degradation behaviors of zinc-based alloys prepared by selective laser melting. *Mater Res Express*. 2022;9(8):086511. doi: 10.1088/2053-1591/ac88b7

26. Yang Y, Yuan F, Gao C, et al. A combined strategy to enhance the properties of Zn by laser rapid solidification and laser alloying. *J Mech Behav Biomed Mater*. 2018;82:51-60. doi: 10.1016/j.jmbbm.2018.03.018

27. Qin Y, Liu A, Guo H, et al. Additive manufacturing of Zn-Mg alloy porous scaffolds with enhanced osseointegration: *in vitro* and in vivo studies. *Acta Biomater*. 2022;145:403-415. doi: 10.1016/j.actbio.2022.03.055

28. Bai J, Xu Y, Fan Q, et al. Mechanical properties and degradation behaviors of Zn-*x*Mg alloy fine wires for biomedical applications. *Scanning*. 2021;2021:4831387. doi: 10.1155/2021/4831387

29. Dambatta MS, Izman S, Kurniawan D, Farahany S, Yahaya B, Hermawan H. Influence of thermal treatment on microstructure, mechanical and degradation properties of Zn–3Mg alloy as potential biodegradable implant material. *Mater Des*. 2015;85:431-437. doi: 10.1016/j.matdes.2015.06.181

30. Chua C, Sing SL, Chua CK. Characterisation of in-situ alloyed titanium-tantalum lattice structures by laser powder bed fusion using finite element analysis. *Virtual Phys Prototyp*. 2023;18(1):e2138463. doi: 10.1080/17452759.2022.2138463

31. Yao C, Wang Z, Tay SL, Zhu T, Gao W. Effects of Mg on microstructure and corrosion properties of Zn–Mg alloy. *J Alloys Compd*. 2014;602:101-107. doi: 10.1016/j.jallcom.2014.03.025

32. Dambatta MS, Izman S, Hermawan H, Kurniawan D. Influence of heat treatment cooling mediums on the degradation property of biodegradable Zn-3Mg alloy. *Adv Mat Res*. 2014;845:7-11. doi: 10.4028/www.scientific.net/AMR.845.7

33. Dambatta MS, Izman S, Hermawan H, Kurniawan D. Effect of heat treatment on microstructure homogeneity of Zn-3Mg alloy. *Appl Mech Mater*. 2014;493:777-782. doi: 10.4028/www.scientific.net/AMM.493.777

34. Cui L, Zhang Z, Chen X. Microstructure and mechanical properties of novel Al–Cu–Mg–Zn lightweight entropy alloys for elevated-temperature applications. *Mater Charact*. 2023;200:112927. doi: 10.1016/j.matchar.2023.112927

35. Yang Y, Lu C, Shen L, Zhao Z, Peng S, Shuai C. In-situ deposition of apatite layer to protect Mg-based composite fabricated via laser additive manufacturing. *J Magnes Alloy*. 2023;11(2):629-640. doi: 10.1016/j.jma.2021.04.009

36. Parsons EM, Shaik SZ. Additive manufacturing of aluminum metal matrix composites: mechanical alloying of composite powders and single track consolidation with laser powder bed fusion. *Addit Manuf*. 2022;50:102450. doi: 10.1016/j.addma.2021.102450

37. Bouabbou A, Vaudreuil S. Understanding laser-metal interaction in selective laser melting additive manufacturing through numerical modelling and simulation: a review. *Virtual Phys Prototyp*. 2022;17(3):543-562. doi: 10.1080/17452759.2022.2052488

38. Zheng YF, Gu XN, Witte F. Biodegradable metals. *Mat Sci Eng R*. 2014;77:1-34. doi: 10.1016/j.mser.2014.01.001

39. Ye L, Huang H, Sun C, et al. Effect of grain size and volume fraction of eutectic structure on mechanical properties and corrosion behavior of as-cast Zn–Mg binary alloys. *J Mater Res Technol*. 2022;16:1673-1685. doi: 10.1016/j.jmrt.2021.12.101

40. Gao C, Li S, Liu L, et al. Dual alloying improves the corrosion resistance of biodegradable Mg alloys prepared by selective laser melting. *J Magnes Alloy*. 2021;9(1):305-316. doi: 10.1016/j.jma.2020.03.016

41. Hosking NC, Ström MA, Shipway PH, Rudd CD. Corrosion resistance of zinc–magnesium coated steel. *Corros Sci*. 2007;49(9):3669-3695. doi: 10.1016/j.corsci.2007.03.032

42. Prosek T, Thierry D, Taxén C, Maixner J. Effect of cations on corrosion of zinc and carbon steel covered with chloride deposits under atmospheric conditions. *Corros Sci*. 2007;49(6):2676-2693. doi: 10.1016/j.corsci.2006.11.004

43. Hausbrand R, Stratmann M, Rohwerder M. Corrosion of zinc–magnesium coatings: mechanism of paint delamination. *Corros Sci*. 2009;51(9):2107-2114. doi: 10.1016/j.corsci.2009.05.042

44. Falk T, Svensson JE, Johansson LG. The influence of CO_2 and NaCl on the atmospheric corrosion of zinc: a laboratory study. *J Electrochem Soc*. 1998;145(9):2993. doi: 10.1149/1.1838753

45. Ralston KD, Birbilis N, Davies C. Revealing the relationship between grain size and corrosion rate of metals. *Scr Mater*. 2010;63(12):1201-1204. doi: 10.1016/j.scriptamat.2010.08.035

46. Pachla W, Przybysz S, Jarzębska A, et al. Structural and mechanical aspects of hypoeutectic Zn–Mg binary alloys for biodegradable vascular stent applications. *Bioact Mater*. 2021;6(1):26-44. doi: 10.1016/j.bioactmat.2020.07.004

47. Li HF, Xie XH, Zheng YF, et al. Development of biodegradable Zn-1X binary alloys with nutrient alloying elements Mg, Ca and Sr. *Sci Rep*. 2015;5(1):10719. doi: 10.1038/srep10719

48. García-Mintegui C, Córdoba LC, Buxadera-Palomero J, et al. Zn-Mg and Zn-Cu alloys for stenting applications: from nanoscale mechanical characterization to *in vitro* degradation and biocompatibility. *Bioact Mater*. 2021;6(12):4430-4446. doi: 10.1016/j.bioactmat.2021.04.015